Monthly Notices of the ROYAL ASTRONOMICAL SOCIETY

MNRAS **458,** 2288–2302 (2016) doi:10.1093/mnras/stw444
Advance Access publication 2016 March 1

The dust covering factor in active galactic nuclei

Marko Stalevski,[1,2,3,4★] Claudio Ricci,[4,5,6] Yoshihiro Ueda,[4] Paulina Lira,[1] Jacopo Fritz[7] and Maarten Baes[3]

[1]*Departamento de Astronomia, Universidad de Chile, Camino El Observatorio 1515, Casilla 36-D Santiago, Chile*
[2]*Astronomical Observatory, Volgina 7, 11060 Belgrade, Serbia*
[3]*Sterrenkundig Observatorium, Universiteit Gent, Krijgslaan 281-S9, Gent B-9000, Belgium*
[4]*Department of Astronomy, Kyoto University, Oiwake-cho, Sakyo-ku, Kyoto 606-8502, Japan*
[5]*Instituto de astrofísica, Pontificia Universidad Catolica de Chile, Casilla 306, Santiago 22, Chile*
[6]*EMBIGGEN Anillo, Casilla 160-C Concepcion, Chile*
[7]*Instituto de Radioastronomía y Astrofísica, IRyA, UNAM, Campus Morelia, A.P. 3-72, C.P. 58089, Mexico*

Accepted 2016 February 22. Received 2016 February 22; in original form 2015 November 17

ABSTRACT

The primary source of emission of active galactic nuclei (AGNs), the accretion disc, is surrounded by an optically and geometrically thick dusty structure ('the so-called dusty torus'). The infrared radiation emitted by the dust is nothing but a reprocessed fraction of the accretion disc emission, so the ratio of the torus to the AGN luminosity ($L_{\rm torus}/L_{\rm AGN}$) should corresponds to the fraction of the sky obscured by dust, i.e. the covering factor. We undertook a critical investigation of the $L_{\rm torus}/L_{\rm AGN}$ as the dust covering factor proxy. Using state-of-the-art 3D Monte Carlo radiative transfer code, we calculated a grid of spectral energy distributions (SEDs) emitted by the clumpy two-phase dusty structure. With this grid of SEDs, we studied the relation between $L_{\rm torus}/L_{\rm AGN}$ and the dust covering factor for different parameters of the torus. We found that in the case of type 1 AGNs the torus anisotropy makes $L_{\rm torus}/L_{\rm AGN}$ underestimate low covering factors and overestimate high covering factors. In type 2 AGNs $L_{\rm torus}/L_{\rm AGN}$ always underestimates covering factors. Our results provide a novel easy-to-use method to account for anisotropy and obtain correct covering factors. Using two samples from the literature, we demonstrated the importance of our result for inferring the obscured AGN fraction. We found that after the anisotropy is properly accounted for, the dust covering factors show very weak dependence on $L_{\rm AGN}$, with values in the range of $\approx$0.6–0.7. Our results also suggest a higher fraction of obscured AGNs at high luminosities than those found by X-ray surveys, in part owing to the presence of a Compton-thick AGN population predicted by population synthesis models.

Key words: radiative transfer – galaxies: active – galaxies: nuclei – galaxies: Seyfert.

1 INTRODUCTION

Active galactic nuclei (AGN) are powered by accretion of gas on to a supermassive black hole (Lynden-Bell 1969). The electromagnetic emission of AGN is characterized by a very strong UV/optical and X-ray continuum coming from the accretion disc and its corona. In the standard unified model of AGNs this central region is surrounded by a geometrically and optically thick dusty structure, whose exact geometry is unknown but is commonly approximated by a clumpy, toroidal distribution and referred to as 'the dusty torus' (see reviews by Antonucci 1993 and Netzer 2015). Part of the accretion disc continuum is radiated towards the dust-free cone cavity formed along the torus axis of symmetry and escapes freely (see Fig. 1). The remaining of the primary continuum goes inside the dusty region where, if the dust is optically thick, it is entirely reprocessed by scattering and absorption from dust grains, and is eventually re-emitted in the infrared (IR). Then from simple geometrical considerations it follows that the ratio of the torus to AGN luminosity ($L_{\rm torus}/L_{\rm AGN}$) corresponds to the fraction of the sky covered by the dust, i.e. the *covering factor* (CF). This CF is directly related to the probability to observe an AGN as a type 1 or type 2, so $L_{\rm torus}/L_{\rm AGN}$ lends itself naturally for the task of inferring the fraction of obscured AGNs as a function of luminosity or redshift, making it also a valuable tool for studying cosmological evolution of AGNs.

A number of works inferring the CF from $L_{\rm torus}/L_{\rm AGN}$ are present in the literature. The sample analysed by (Maiolino et al. 2007) combined high-luminosity quasars and low-luminosity type-1 AGNs for

★ E-mail: marko.stalevski@gmail.com

© 2016 The Authors
Published by Oxford University Press on behalf of the Royal Astronomical Society

Downloaded from http://mnras.oxfordjournals.org/ at UNIVERSIDAD DE CHILE on August 9, 2016

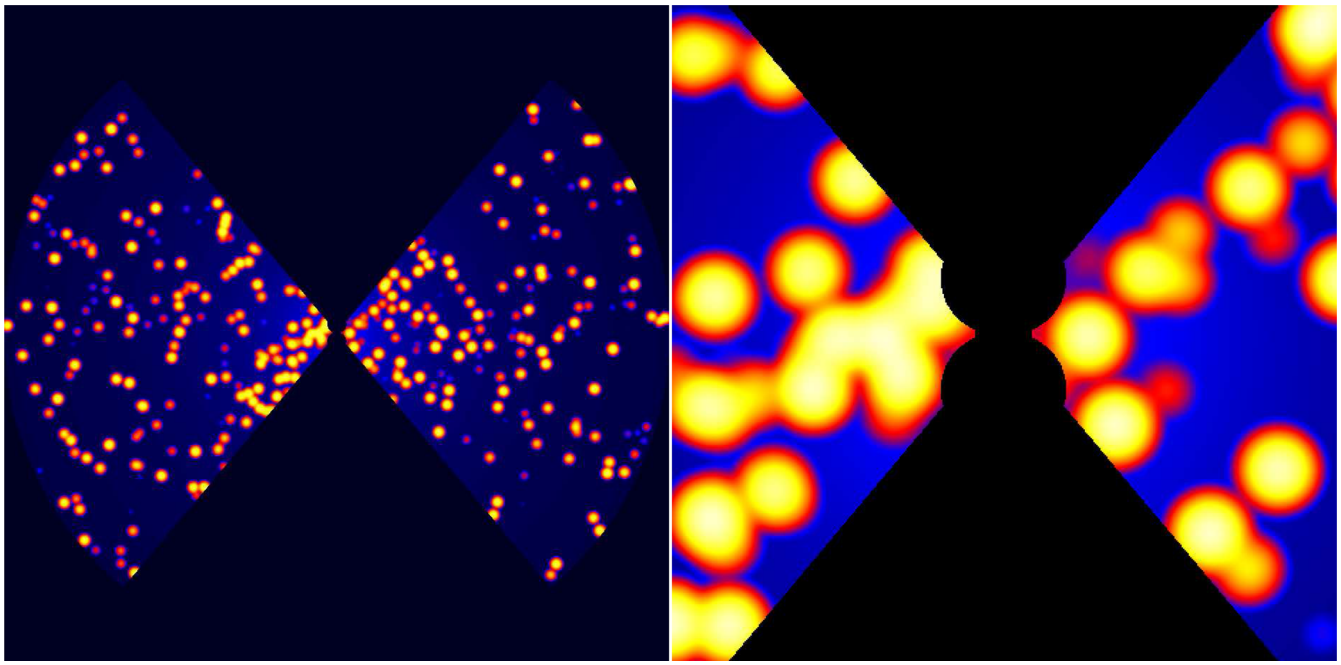

Figure 1. Dust density map of the vertical *xz* plane (left) and zoom-in (right) of the inner region revealing the inner wall reshaped to account for anisotropic irradiation by the accretion disc. High-denisity clumps are seen in yellow, while the low-density interclump dust is in shades of blue. Presented in logarithmic colour scale.

a total number of 58 objects with *Spitzer*-IRS data. Treister, Krolik & Dullemond (2008) estimated CFs of 230 type 1 AGNs selected from several surveys, based on flux measured in a single *Spitzer* band (24 μm) and employing radiative transfer solutions. Numerous authors derived CFs by fitting torus emission models to the spectral energy distributions (SEDs) of type 1 and type 2 AGNs (e.g. Fritz, Franceschini & Hatziminaoglou 2006; Hatziminaoglou, Fritz & Jarrett 2009; Mor, Netzer & Elitzur 2009; Mor & Trakhtenbrot 2011; Alonso-Herrero et al. 2011; Ramos-Almeida et al. 2011; Mor & Netzer 2012; Mateos et al. 2015, 2016). Roseboom et al. (2013) used various combinations of a hot blackbody, and a warm dusty torus, to fit broad-band NIR–MIR data in a large sample of *WISE*-selected sources. Using broad-band JHK and *Spitzer* mid-infrared (MIR) data, Lusso et al. (2013) analysed the obscured fraction for a sample of 513 type 1 AGNs from the XMM-COSMOS survey. Netzer et al. (2016) use combined *Herschel*/SPIRE and *WISE* observations of 35 high-redshift AGNs. Most of these works have broadly consistent results, finding general trends of decreasing obscured fraction with increasing $L_{\rm AGN}$ (see the discussion and comparison in Lusso et al. 2013). The exception is the work by Netzer et al. (2016) who infer CFs consistent with no clear evolution with nuclear luminosity, within the uncertainties for the bolometric correction factor.

However, the above reasoning for interpreting $L_{\rm torus}/L_{\rm AGN}$ as the CF is strictly valid only if both the disc and the surrounding dusty structure are emitting isotropically. The standard geometrically thin and optically thick disc cannot emit isotropically (Netzer 1987). To obscure the central region, as required by the unification model, the dusty torus has to be optically thick. Furthermore, it has to be optically thick to its own radiation in the MIR, to produce the observed appearance of the silicate feature in emission and absorption (in the first case it can often be weak or flat) in type 1 and 2 AGNs. As such, the dusty torus will inevitably emit anisotropically as well. This means that the observed $L_{\rm torus}/L_{\rm AGN}$ will not represent the actual CF, but it will rather be convolved with the aforementioned effects due to the anisotropic nature of the accretion disc and the dusty torus emission. Disentangling these effects to reveal the true CF cannot be done analytically. Instead, authors usually discuss their results within the limiting cases of total isotropy and total anisotropy (e.g. Lusso et al. 2013; Netzer 2015). The disadvantage of this approach is that these limits represent two extremes between which considerable uncertainty remains.

Given the complex nature of the problem, the most promising way to properly account for these effects is to realistically simulate reprocessing of the accretion disc radiation as it travels through the dusty medium and reconstruct the resulting IR emission. This is exactly what is our approach in this work. We employ a state-of-the-art radiative transfer code based on the Monte Carlo technique (MCRT) to calculate a grid of SEDs for an inhomogeneous dusty torus for different values of CF and other parameters. This grid of SEDs allow us to study the relation between $L_{\rm torus}/L_{\rm AGN}$ and the CF. We then use the obtained relations to correct the observed $L_{\rm torus}/L_{\rm AGN}$ and recover the actual CFs. A somewhat similar approach was adopted by Treister et al. (2008) who used radiative transfer emission models to relate the observed ratio of 24 μm and bolometric luminosities to the obscured fraction of AGN sky. However, the realization of our model is substantially different, we cover a larger parameter space in our simulations, and we focus on the deeper understanding of the relation between $L_{\rm torus}/L_{\rm AGN}$ and the dust CF, by isolating the different effects that contribute to the torus anisotropy.

In Section 2 we overview our method and provide the details of our dusty torus model. We present the relevant properties of the calculated grid of model SEDs in Section 3 and examine in detail the obtained relations between $L_{\rm torus}/L_{\rm AGN}$ and the CF. In Section 4 we apply our method on two samples from the literature and discuss implications for inferring the obscured fraction of AGNs as a function of luminosity. The paper is concluded with a summary of our main findings in Section 5.

Downloaded from http://mnras.oxfordjournals.org/ at UNIVERSIDAD DE CHILE on August 9, 2016

2 METHOD AND MODEL

2.1 Method

A considerable source of uncertainties in inferring the dust CF from $L_{\rm torus}/L_{\rm AGN}$ comes from the bolometric correction factor which is needed to estimate $L_{\rm AGN}$. According to Marconi et al. (2004), this correction factor for luminosity in optical regime decreases with increasing $L_{\rm AGN}$. However, the correction factors adopted by different authors differ significantly (e.g. Shen et al. 2011; Runnoe, Brotherton & Shang 2012; Trakhtenbrot & Netzer 2012; Krawczyk et al. 2013). In fact, Netzer et al. (2016) argue that earlier results of IR-derived CFs are biased by the inconsistent use of various bolometric correction factors. This issues is beyond the scope of this work; we will assume that $L_{\rm AGN}$ can be constrained with satisfactory accuracy and focus only on $L_{\rm torus}$ and uncertainties due to anisotropic emission.

Our approach to the problem is the following. We calculate a grid of IR SEDs emitted by the dusty torus for a given central source luminosity ($L_{\rm AGN}$) with anisotropic emission pattern. Then, we integrate the IR flux of the model SEDs, convert it to luminosity, and compare $L_{\rm torus}/L_{\rm AGN}$ to the true CF, which in our model corresponds to the opening angle of the torus. By means of this comparison we investigate how the $L_{\rm torus}/L_{\rm AGN}$ ratio deviates from the actual CF, and how this deviation depends on different parameters of the obscuring dust. Apart from the total infrared emission, we also test near-infrared (NIR), MIR, far-infrared (FIR) and individual fluxes at 6.7 μm and 12 μm as proxies of the dust CF (e.g. Maiolino et al. 2007).

2.2 The SKIRT CODE

To calculate model SEDs we make use of SKIRT,[1] a state-of-the-art code for simulating continuum radiation transfer in dusty astrophysical systems (Baes et al. 2003, 2011; Camps & Baes 2015). SKIRT employs the Monte Carlo technique to emulate the relevant physical processes including multiple anisotropic scattering, absorption and (re-)emission by the dust, and handles any 3D geometry without limitation (Camps, Baes & Saftly 2013; Saftly et al. 2013; Saftly, Baes & Camps 2014). The code is being used for a variety of applications, including study of the dust energy balance in spiral galaxies (Baes et al. 2010; De Looze et al. 2012a,b; De Geyter et al. 2015), and the investigation of the structure and observable properties of AGN dusty tori (Stalevski et al. 2012a,b,c; Popović et al. 2012).

2.3 The dusty torus as a two-phase medium

We model the distribution of the dust in the torus as a two-phase medium, consisting of a large number of high-density clumps embedded in a smooth dusty component of low density. Previously, we have found that an advantageous property of such two-phase medium is that it can produce attenuated silicate features, while at the same time have a pronounced NIR emission, which is challenging for both smooth and clumpy models alone (Stalevski et al. 2012a,b). Since then, several lines of evidences were found providing further supporting that the torus is indeed a multiphase structure. Studies using hydrodynamical simulations and taking into account other processes such as self-gravity of the gas, radiative cooling and heating due to supernovae or accretion disc, found that the interstellar medium around the AGN would result in a multiphase filamentary structure (Wada, Papadopoulos & Spaans 2009; Wada 2012). Using the two-phase model SEDs grid of Stalevski et al. (2012b), Roseboom et al. (2013) were able to reproduce the observed ratio of NIR to total IR luminosity in a large sample of sources selected from the *WISE* catalogue, something which models consisting of only clumps are not able to achieve. Analysing a large AGN sample from the *WISE* catalogue, Assef et al. (2013) found that the observed reddening distribution can be explained by a torus-like structure in which thick dust clouds are embedded in a diffuse intercloud dust medium. Another indication of a presence of smooth, low-density intercloud medium comes from constant baseline level absorption, between the strong absorption events, in type 2 AGN well-monitored with *RXTE* (Markowitz, Krumpe & Nikutta 2014). Studying variable reddening in Narrow-line Seyfert 1, Leighly et al. (2015) concluded that it is 'plausible that the occulting material is a clump embedded in a larger region of dusty gas responsible for the longer time-scale reddening changes, and both are associated with the torus'. Finally, such two-phase structures have been actually observed in the central regions of Milky Way (the so-called Central Molecular Zone and Circumnuclear Disk) and it has been suggested that they represent a remnant of a dusty torus that may have played a role in past AGN phases of our Galaxy (Molinari et al. 2011; Ponti et al. 2013).

2.4 Model parameters

The dusty torus model from this work shares a common ground with the one presented in Stalevski et al. (2012b), but with a number of changes and improvements. Here we describe the most important properties.

The primary source of emission is the accretion disc, approximated by a central point source with anisotropic emission distributed as proposed by Netzer (1987):

$$L(\theta) \propto \cos\theta(2\cos\theta + 1), \tag{1}$$

where θ is polar angle of the coordinate system. The first factor in this equation describes the change in the projected surface area and the second factor accounts for the limb darkening effect. The SED of the accretion disc is described by the following composition of power laws, in agreement with theoretical predictions and observational evidences (e.g Hubeny et al. 2001; Davis & Laor 2011; Slone & Netzer 2012; Capellupo et al. 2015):

$$\lambda L_\lambda \propto \begin{cases} \lambda^{1.2} & 0.001 \leq \lambda <\leq 0.01\ [\mu\text{m}] \\ \lambda^{0} & 0.01 < \lambda \leq 0.1\ [\mu\text{m}] \\ \lambda^{-0.5} & 0.1 < \lambda \leq 5\ [\mu\text{m}] \\ \lambda^{-3} & 5 < \lambda \leq 50\ [\mu\text{m}] \end{cases} \tag{2}$$

We approximate the spatial distribution of dust with a flared disc whose geometry is defined by the inner ($R_{\rm in}$) and outer radii ($R_{\rm out}$) and the half opening angle (Δ). The inner radius is determined by the dust sublimation temperature for a given $L_{\rm AGN}$ (Barvainis 1987):

$$\left(\frac{R_{\rm in}}{\rm pc}\right) \simeq 1.3 \left(\frac{L_{\rm AGN}}{10^{46}\text{erg s}^{-1}}\right)^{0.5} \left(\frac{T_{\rm sub}}{1500\text{K}}\right)^{-2.8}, \tag{3}$$

assuming an average dust grain size of 0.05 μm. The accretion disc emission described by equation (1) is highly anisotropic, with the strongest emission perpendicular to the disc and none in the

[1] http://www.skirt.ugent.be

Downloaded from http://mnras.oxfordjournals.org/ at UNIVERSIDAD DE CHILE on August 9, 2016

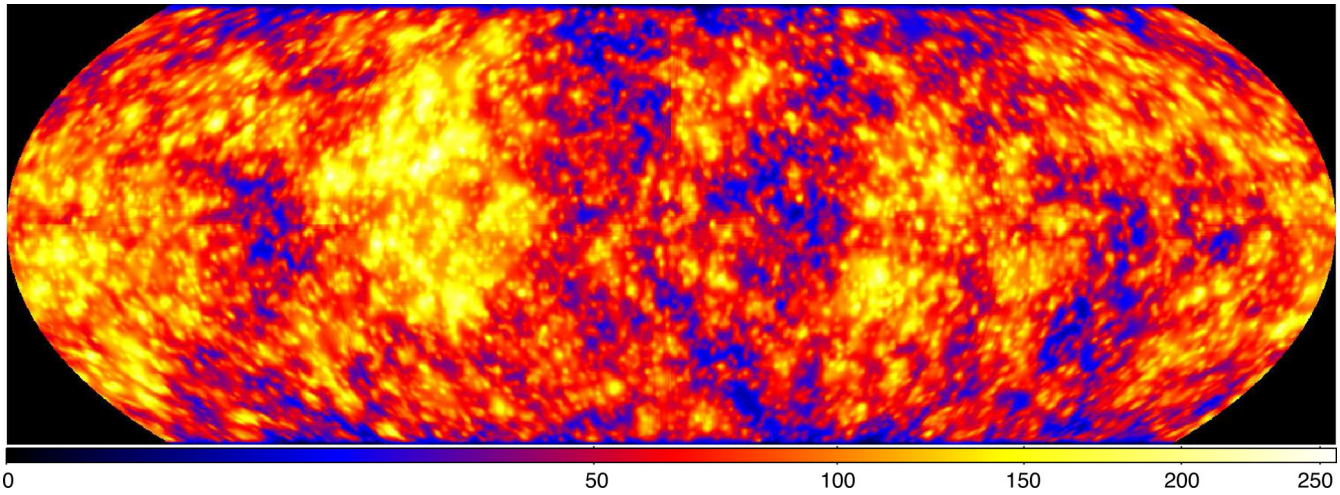

Figure 2. Optical depth map of the sky in the V band, as it would be seen from the centre of AGN for the density profile show in Fig. 1. The dark blue areas are the ones with the lowest optical depth $\tau_V \approx 5$–10. Presented in square root colour scale.

equatorial plane. The inner radius in this case cannot be constant but must follow the same dependence with polar angle:

$$R_{\rm in} \propto R_{\rm iso}[\cos\theta(2\cos\theta + 1)]^{0.5}, \quad (4)$$

where $R_{\rm iso}$ is inner radius in the case of isotropic disc emission.

In the literature, some authors use the term 'half opening angle' to describe the opening of the dust-free cone measured from the polar axis, while other authors use it as a measure of the dust-filled zone, from the equator to the edge of the torus. To remain consistent with the notation used in our original model in Stalevski et al. (2012b), we choose the latter definition, measuring the half opening angle from the equator to the flaring edge. This parameter is linked to the CF by a simple relation:

$$\mathrm{CF} = \sin(\Delta). \quad (5)$$

Dust is distributed according to a law that allows a density gradient along the radial direction (r) and with polar angle (θ):

$$\rho\,(r,\theta) \propto r^{-p} e^{-q|\cos\theta|}, \quad (6)$$

where r and θ are coordinates in the adopted coordinate system. Dust in our model is modelled as a mixture of silicate and graphite grains with classical MRN size distribution (Mathis, Rumpl & Nordsieck 1977), with the normalization factors for size distribution from Weingartner & Draine (2001), and with optical properties taken from Laor & Draine (1993) and Li & Draine (2001).

The parameters defining the clumpiness are the total number of clumps ($N_{\rm cl}$) and the fraction of total dust mass of the torus locked up inside clumps ($f_{\rm cl}$). The clumps are allowed to overlap and form complex structures. For density profile of individual clumps we assume the standard smoothing kernel with compact support, providing computational accuracy and efficiency (Monaghan & Lattanzio 1985; Springel 2010):

$$W(u) = \frac{8}{\pi}\begin{cases} 1 - 6u^2 + 6u^3, & 0 \le u \le \frac{1}{2}, \\ 2\,(1-u)^3\,, & \frac{1}{2} < u \le 1, \\ 0, & u > 1, \end{cases} \quad (7)$$

with u being the radius normalized by the scale radius of a clump, h. Fig. 1 illustrates the geometry and dust distribution in a typical two-phase model. For details on the implementation of such a clumpy geometry see Baes & Camps (2015).

The total amount of dust is set by the equatorial optical depth at 9.7 μm ($\tau_{9.7}$) of the underlying density profile defined by equation (6), before applying the algorithm that generates clumps. After redistributing the dust into a clumpy two-phase medium, the optical depth along a given line of sight can vary significantly, mostly depending on the number of clumps intercepted, as seen in the optical depth map shown in Fig. 2. In this map, dark blue areas represent clump-free lines of sight. The adopted values of the parameters defining clumpiness result in the contrast (i.e. ratio) between the high and low dust density phases of ≈100. However, even for such a high contrast, the clump-free lines of sight are still optically thick for the accretion disc radiation ($\tau_V = 5$–10), so the CF still corresponds to the torus opening angle (equation 5).

3 RESULTS AND DISCUSSION

In this section we first present examples of typical model SEDs and images and comment on some of their properties relevant for this work. Then we present and analyse the relation between $L_{\rm torus}/L_{\rm AGN}$ and the dust CF.

3.1 Model SEDs and images

In Figs 3 and 4 we present SEDs with typical model parameters adopted for this work. The luminosity of the primary source (the accretion disc) is $L_{\rm AGN} = 10^{11} L_{\odot}$ and the SEDs in all the figures are scaled to a source at a distance of 10 Mpc. We remind the reader of some important scaling properties of dust radiative transfer models: when a change of the primary source luminosity is accompanied by a required change of the sublimation radius (equation 3), while keeping the optical depth and the outer-to-inner radius ratio ($R_{\rm out}/R_{\rm in}$) constant, the shape of the resulting SED will remain exactly the same, only scaled along the flux axis (Ivezic & Elitzur 1997; Fritz et al. 2006). Also, it is trivial to rescale the model flux to any given distance between the observer and the source. Thus, model SEDs obtained with MCRT method are applicable to any given source luminosity and distance (see Hönig & Kishimoto 2010 for more details).

Graphite and silicate grains have different sublimation temperatures, with graphite being able to withhold higher ones and thus survive closer in. Also, larger grains are cooling more efficiently

Downloaded from http://mnras.oxfordjournals.org/ at UNIVERSIDAD DE CHILE on August 9, 2016

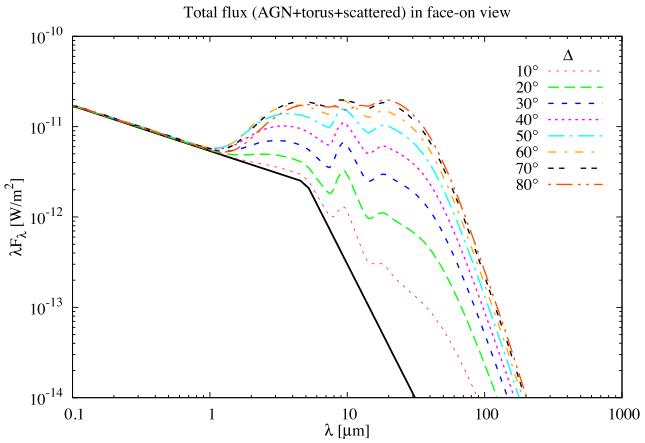

Figure 3. SEDs for different values of the torus half opening angle Δ (i.e. the CF). The solid line is the central source (accretion disc) SED.

than smaller grains. Hence, rather than a well-defined $R_{\rm in}$ determined by the sublimation radius, we expect to have a sublimation zone, from larger to smaller grains and from graphite to silicate (see e.g. Kishimoto et al. 2007; Mor & Netzer 2012). However, setting up the sublimation zone is non-trivial, as radiative transfer and shielding effects between the different zones must be taken into account and the simulation has to be iterated until each zone reaches its sublimation temperature (Fritz et al. 2006). A proper treatment of sublimation zone is beyond the scope this work and will be part of a future investigation. For this work we choose the same inner radius for both graphite and silicates corresponding to an average temperature of ≈1250 K of the regions located closest the central source ($R_{\rm iso}$ = 0.21 pc; the actual $R_{\rm in}$ is set by equation 4) As a consequence, this may result in lower NIR emission in our models than in some observed composite SEDs, such as those found in Mor & Netzer (2012). On the other hand, Roseboom et al. (2013) found that the observed ratio of NIR to total IR luminosity in their *WISE*-selected sample is easily achievable by our models presented in Stalevski et al. (2012b). In any case, we base our main results on the total IR luminosity as the CF proxy. The eventual lack of hot dust may results in redistribution of flux between NIR, MIR and FIR, but the total torus luminosity would remain the same; we remind the reader that the total luminosity radiated by the torus is completely determined by the fraction of accretion disc radiation that penetrates the torus through the dusty interface.

Finally, in the examples shown here, the outer torus radius is 5 pc, the dust density law (equation 6) is taken to have an exponent $p = 1$ for the radial part and to be constant with polar angle ($q = 0$), and the edge-on optical depth ($\tau_{9.7}$) takes values between 0.1 and 10. Scale radius of a clump (h) is 0.4 pc. Only ≈3 per cent of the total dust mass is in the low-density phase ($f_{\rm cl} \approx 0.97$).

The full line in Fig. 3 represents the accretion disc SED; the remaining lines are the SEDs of our torus model for different half opening angles in the range of Δ = 10°–80°. The model SEDs have the general properties consistent with those previously presented in Stalevski et al. (2012b). It is worth inspecting closer the SEDs of models with low CFs (Δ = 10°, 20°). A disc with an anisotropic luminosity as described by equation (1) emits very little in the directions close to equatorial plane. The tori with small CFs thus receive very little illumination and as a consequence have very weak IR dust signatures. In fact, IR-based selection would most likely completely miss these objects.

In Fig. 4 we show how the SEDs change as a function of the optical depth, from very low to high. Here we draw the attention of the reader to the three cases of low optical depths in the MIR, $\tau_{9.7}$ = 0.1, 0.5, 1. We see that these three cases result in strong 10 μm silicate emission feature even in edge-on view. As type 2 AGNs, with a few exceptions, show this feature in absorption, we consider these cases to be unrealistic and include them only for the sake of completeness, and to isolate the effects of the accretion disc and dust anisotropy.

We also present the examples of model images at different wavelengths and temperature maps. The first panel from the left in Fig. 5 displays the V-band image where scattered light is dominant. The remaining panels display images of hot and warm dust at 4.6, 9.6 and 12 μm. Fig. 6 shows the temperature distribution in the xz (left) and yz (right) planes. The patterns seen in these maps are formed by alternation of clump-free lines of light propagation and regions shadowed by the clumps.

3.2 $L_{\rm torus}/L_{\rm AGN}$ as a CF proxy: type 1 AGN case

Now we will investigate the relation between $L_{\rm torus}/L_{\rm AGN}$ and the actual CF of the dust, and its dependence on the different parameters of the torus, focusing on the case of type 1 AGNs. All the results

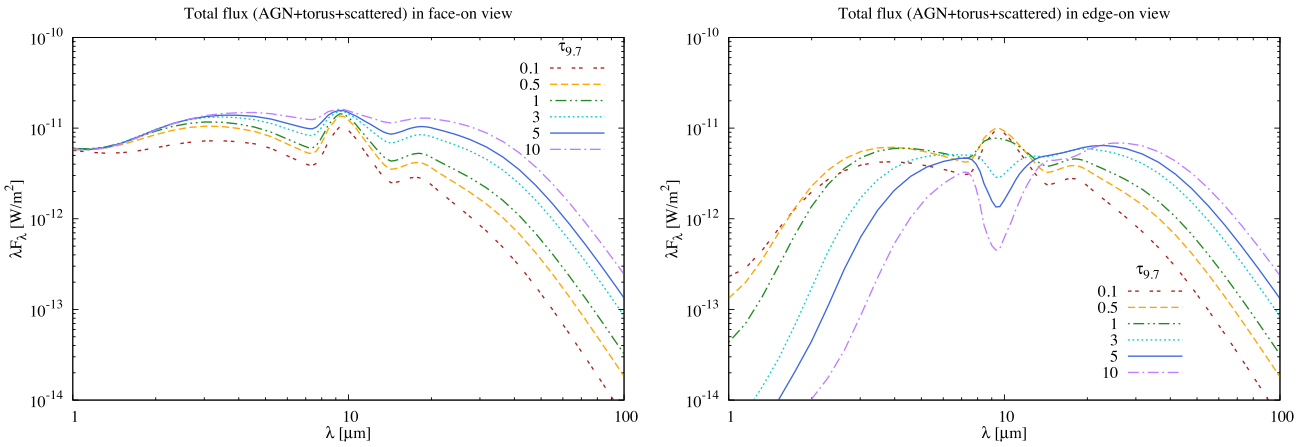

Figure 4. Illustrating the change of the model SEDs for different optical depths along the equatorial line of sight ($\tau_{9.7}$) for face-on (left) and edge-on (right) views. The half opening angle is fixed at Δ = 50°. Note how the models with low optical depth (0.1–1) result in strong 10 μm silicate emission feature even in edge-on views.

Downloaded from http://mnras.oxfordjournals.org/ at UNIVERSIDAD DE CHILE on August 9, 2016

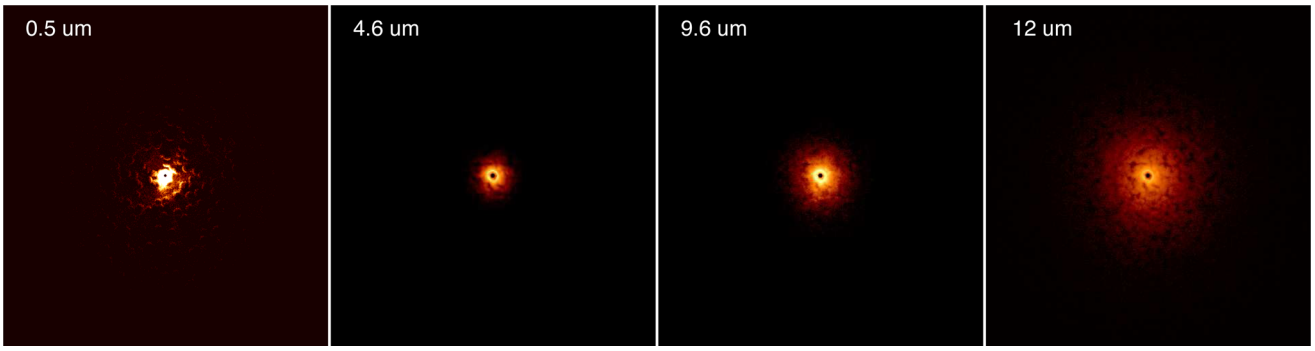

Figure 5. Flux images of the torus in face-on view at different wavelengths, from the optical to MIR. In the left-hand panel we see scattered light in optical; continuing to the right, the other panels show hot to warm dust emission, seen in the NIR–MIR regimes. Presented in logarithmic colour scale with arbitrary cut offs in each image.

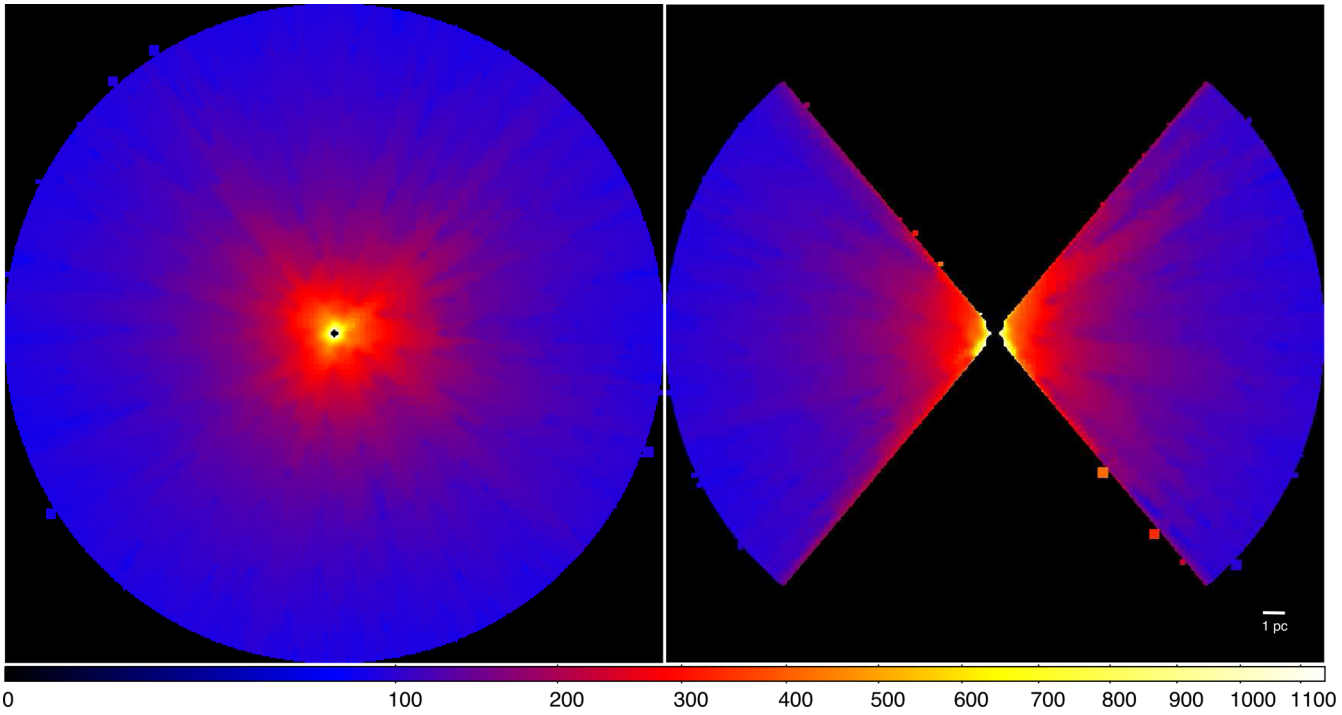

Figure 6. Temperature maps of the *xy* (left) and *xz* (right) planes in the Kelvin scale. Presented in square root colour scale. The alternation of clump-free lines of light propagation and regions in shadow behind the clumps is visible. White line in the lower right corner represents 1 pc, which is equivalent to $\approx 2R_{\rm sub}$ for a given luminosity, $L_{\rm AGN} = 10^{11} L_{\odot}$.

presented in this section are obtained for face-on viewing angle $i = 0^{\circ}$. However, the torus IR SEDs change only minimally with changing viewing angle, as long as it still provides a dust-free (type 1) line of sight (Stalevski et al. 2012b). Thus, the results presented here are valid for type 1 AGNs in general irrespective of their inclination.

3.2.1 *The total infrared emission*

We start by examining Fig. 7. The horizontal axis in this plot denotes the CF (defined by the parameter Δ, the half opening angle) while on the vertical axis we plot the $L_{\rm torus}/L_{\rm AGN}$ ratio. Both Δ and $L_{\rm AGN}$ are input parameters in the model. $L_{\rm torus}$ is measured from the model SED by simply integrating the dust flux over the entire wavelength range and converting it to luminosity (by multiplying it by 4π and the square of the distance to the source). The integration is done over the entire wavelength range of the simulation, but the same results are obtained if the integration is limited to the range in which dust emission is significant, 1–100 μm. To facilitate a visual inspection, we include the identity 1:1 line in the plots. If the $L_{\rm torus}/L_{\rm AGN}$ ratio is a perfect CF proxy, all the points would be found exactly on this line; the further away they are from the line, the less reliable CF proxy it is. The parameters of the models used in this figure correspond to those described in Section 3.1. Through out the text, the expression 'optically thin/thick' refers specifically to the *V* band, while 'MIR thin/thick' refers to 9.7 μm.

Let us first focus on the left-hand panel of Fig. 7, where we explore the effects of iso- and anisotropic disc emission and optical thickness of the obscuring dust. Open symbols with dashed lines correspond to the isotropic disc emission, while solid symbols with solid lines to the anisotropic case. Yellow lines correspond to optically (and MIR)

Downloaded from http://mnras.oxfordjournals.org/ at UNIVERSIDAD DE CHILE on August 9, 2016

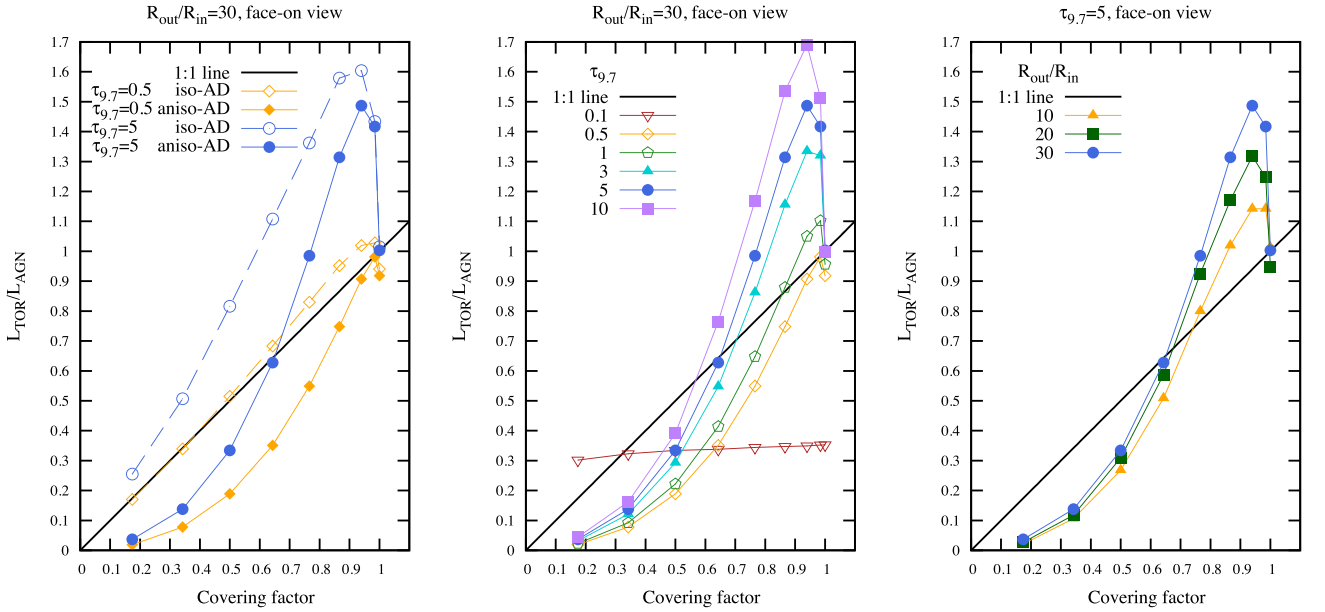

Figure 7. The relation between $L_{\rm torus}/L_{\rm AGN}$ and the CF for the case of face-on view (type 1 AGN). The left-hand panel shows cases of iso- and anisotropic disc emission (open and solid symbols) and optically thin and thick dusty tori (dashed and solid lines). Solid circles with blue lines represent a realistic case of an anisotropic disc and MIR thick dust. The central panel shows the same relation for a range of $\tau_{9.7}$ and with an anisotropic disc in all the cases. Solid symbols denote realistic cases with the dusty torus being moderately to highly MIR thick. Right-hand panel: the same as the central panel but for different values of the $R_{\rm out}/R_{\rm in}$ parameter. The main aspect to note is the that, in the realistic case (e.g. central panel, solid symbols), $L_{\rm torus}/L_{\rm AGN}$ underestimates low CFs and overestimates high CFs.

thin tori, while blue lines to MIR-thick. In the case of isotropically emitting disc surrounded by MIR thin dust, we expect the torus emission to be almost perfectly isotropic and $L_{\rm torus}/L_{\rm AGN}$ to be a very good proxy of the CF. As we see from the plot this is indeed the case (open diamonds with dashed yellow line).

Still considering isotropic disc emission, let us see what happens if the dust surrounding it is MIR thick (open circles with dashed blue line). The torus is now optically thick to its own radiation, resulting in an overall anisotropic emission pattern in which type 1 inclinations have larger IR luminosity than type 2. As a consequence, CFs assessed by $L_{\rm torus}/L_{\rm AGN}$ are overestimated.

Next, we consider the case of anisotropic disc emission (equation 1) with MIR thin dust (solid diamonds with solid yellow line). As mentioned earlier, the reasoning that allows us to interpret the $L_{\rm torus}/L_{\rm AGN}$ as the dust CF is strictly valid only if both the disc and the torus are emitting isotropically. Since we are considering MIR optically thin dust, the torus is indeed emitting isotropically. But since that is not the case with the accretion disc, $L_{\rm torus}/L_{\rm AGN}$ is no longer a valid proxy of the CF: we see that in this case the luminosity ratio underestimates it.

Finally, we examine the realistic case of anisotropic disc emission and MIR thick dust (solid circles with blue solid line). This time we expect to have a combination of the two previous, simplified cases. We see this is indeed the case: we recover the correct CF at $\approx$0.65, while the lower values are underestimated and higher values are overestimated. We notice that $L_{\rm torus}/L_{\rm AGN}$ significantly deviates from the CF and that the difference is not just a systematic shift: the deviation strongly depends on the CF itself. Another undesirable characteristic is the non-uniqueness of the relation in the CF = 0.75–1 range (i.e. there is no one-to-one relation). As the CF is increasing and the dusty structure starts to resemble a sphere, the IR emission becomes more isotropic. Thus the luminosity ratio starts to approach the 1:1 line. The rightmost point in the plot is the case of a model with a CF of 1, i.e. a sphere of dust fully obscuring the central engine. A dusty sphere is indeed emitting isotropically and we recover the correct value of the CF. However, the turning point is at CF $\approx$ 0.94; for such high CF there is a very low probability that the objects would be observed as type 1, so this issue of non-uniqueness will not have a significant impact on actual measurements.

We will now focus on the central panel of Fig. 7. From now on, we are considering only realistic cases of anisotropic disc emission. Here, we look at how the relation between $L_{\rm torus}/L_{\rm AGN}$ and the CF changes over a wide range of dust optical depths, $\tau_{9.7}$ = 0.1–10. In the plot, open symbols denote MIR thin cases, solid symbols MIR thick cases. For $\tau_{9.7} = 0.1$ (red open triangles) the dust is so optically thin that a significant fraction of the AGN emission is able to pass through the torus without being reprocessed by the dust. In this case, the assumption that $L_{\rm torus}/L_{\rm AGN}$ may be used as a CF proxy completely breaks down. Besides, such an optically thin torus cannot provide obscuration required by the unified AGN model.

The following two values of the optical depth we have in our grid ($\tau_{9.7}$ = 0.5, 1) correspond to a dusty region that is opaque to the disc emission. However, as we showed in Fig. 4, in these cases the torus is emitting isotropically, resulting in a strong 10 μm silicate emission feature even for edge-on views. This is in contradiction with observations of type 2s, which, with a few exceptions, show the feature in absorption. Thus, we will be concentrating on the cases of moderate to high optical depths, $\tau_{9.7}$ = 3, 5, 10. Focusing only on these cases, we notice a favourable characteristic: the relation between $L_{\rm torus}/L_{\rm AGN}$ and CF for different optical depths differ significantly from each other only at the higher end of the CFs.

Now we examine the right-hand panel in Fig. 7, where we see how $L_{\rm torus}/L_{\rm AGN}$ behaves for different values of $R_{\rm out}/R_{\rm in}$ parameter (10, 20, 30; from compact to extended tori). Again, we consider

Downloaded from http://mnras.oxfordjournals.org/ at UNIVERSIDAD DE CHILE on August 9, 2016

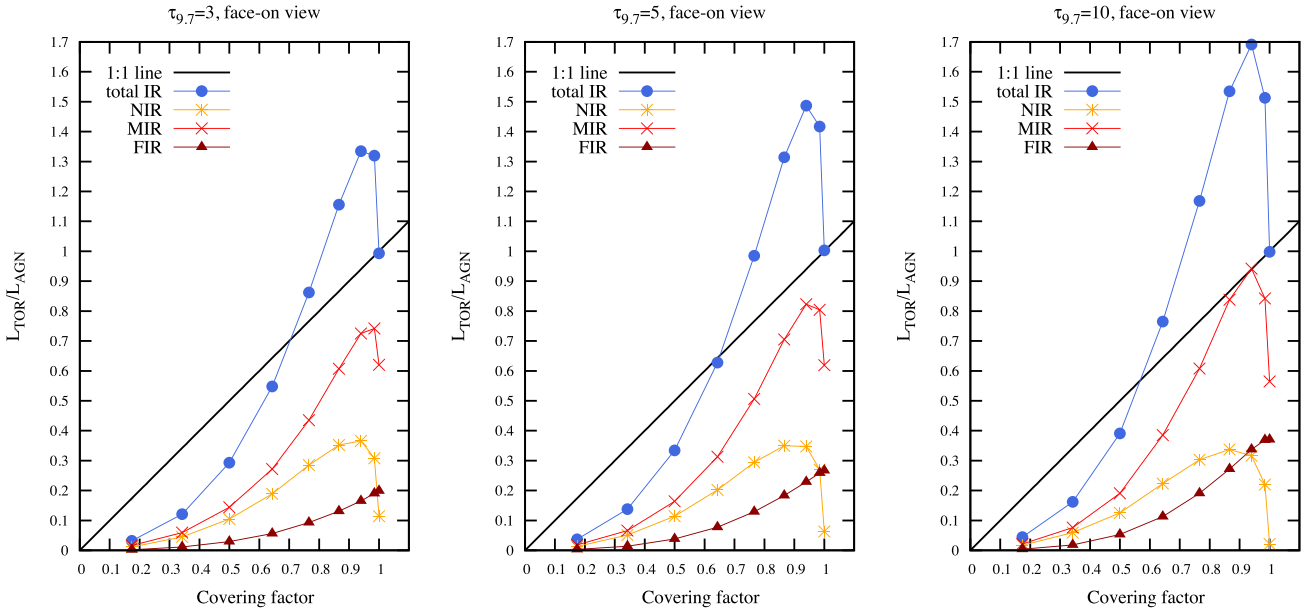

Figure 8. Comparing $L_{\rm torus}/L_{\rm AGN}$ with CFs, using the total torus IR (blue dots), NIR (yellow stars), MIR (red crosses) and FIR (brown triangles) luminosities and for $\tau_{9.7} = 3$, 5, 10 in the left, central and right-hand panels, respectively. Face-on (type 1 AGN) case.

only anisotropic disc emission and moderate optical thickness of the torus ($\tau_{9.7} = 5$). We see that the luminosity reacts to the changes of this parameter in a similar manner as in the previously considered case of different optical depths.

We could demonstrate the same exercise for other torus parameters, but this is not necessary. The exact shape of SED is difficult to predict as it results from the combined effects of all the parameters. However, for this work only the total torus luminosity is relevant, and the level of its anisotropy. The exact level of anisotropy will be determined by an intricate combination of the effects that different parameters have on the radiation transfer. However, the parameter that has the strongest and most direct influence on the anisotropy is the optical depth of the dust. This leads us to a very important point: *all possible combinations of effects other parameters have on the level of anisotropy will be within the limits of the cases of optically thin-to-thick dusty tori.* And we saw that in the realistic range of moderate-to-high optical depth of the dust in the MIR, the different cases diverge significantly from each other only at the high end of the CF values. Thus, we can use the obtained relations to correct the observed $L_{\rm torus}/L_{\rm AGN}$ ratio so that it corresponds more closely to the actual CF. While we may not know the exact optical depth of the objects, we will still be able to robustly constrain the upper and lower CF limits. We will illustrate such an application in Section 4.

3.2.2 *NIR, MIR and FIR emission as CF proxy*

In the previous section we have used the total torus luminosity as a CF proxy. We will now investigate the luminosities of hot (NIR, 1–5 μm), warm (MIR, 5–25 μm) and cold (FIR, 25–380 μm) dust as CF estimators. We confirmed that the results are not sensitive to adjustments of the wavelength range of these three bands (e.g. by changing the mid-far-IR limit to several values between 20 and 100 μm).

In Fig. 8 we show the same relation as in Fig. 7 but for different wavelength bands, where $L_{\rm torus}$ stands for total IR luminosity (blue circles; included for comparison), NIR luminosity (yellow stars), MIR luminosity (red crosses) and FIR luminosity (brown triangles). From left to right, panels correspond to a range of realistic cases of $\tau_{9.7} = 3$, 5, 10. Since NIR–MIR–FIR luminosities represent a fraction of the total $L_{\rm torus}$, they almost always underestimate the CF. We will now have a closer look at each of these.

By examining the yellow stars in all the three panels in Fig. 8 we notice a favourable aspect: $L_{\rm NIR}/L_{\rm AGN}$ has almost no dependence on optical depth (and as we confirmed, neither on other parameters). This means that $L_{\rm NIR}$ could be a very robust CF estimator. However, we must keep in mind that in the NIR band we can have significant contribution by host galaxy stellar emission and/or the accretion disc which must be carefully subtracted. Moreover, even when the stellar component is negligible or properly accounted for, the torus models are not always able to account for a significant fraction of the emission (the so-called NIR excess problem: Polletta et al. 2008; Mor et al. 2009; Deo et al. 2011; Mor & Trakhtenbrot 2011; Lira et al. 2013). The origin of this excess is unclear and plausible sources include hot graphite dust (Mor et al. 2009) and low density interclump dust in the two-phase torus model (Stalevski et al. 2012a,b). Having in mind all this we advise extreme caution if $L_{\rm NIR}/L_{\rm AGN}$ is to be interpreted as the dust CF.

Now we turn our attention to the red crosses in Fig. 8 which represent $L_{\rm MIR}/L_{\rm AGN}$. Again, the CFs are almost always underestimated, except for highly obscured sources in the case of high optical depth (right-hand panel). Similar as when using the total torus luminosity, the cases of different optical depths diverge significantly from each other only for high CFs.

Finally, let us have a look at brown triangles in Fig. 8 which stand for $L_{\rm FIR}/L_{\rm AGN}$. FIR emission mostly comes from the outer regions of the torus where cold dust resides, and from the dark side of the clumps, i.e. those which are not directly illuminated by the central source. But we must keep in mind that in the FIR, the host galaxy contribution is very often dominant over the AGN (e.g. Hatziminaoglou et al. 2008, 2009, 2010). Disentangling the two is a challenging task and introduces more uncertainties. Hence, once again we advise extreme caution if $L_{\rm FIR}/L_{\rm AGN}$ is used to estimate the dust CF.

Downloaded from http://mnras.oxfordjournals.org/ at UNIVERSIDAD DE CHILE on August 9, 2016

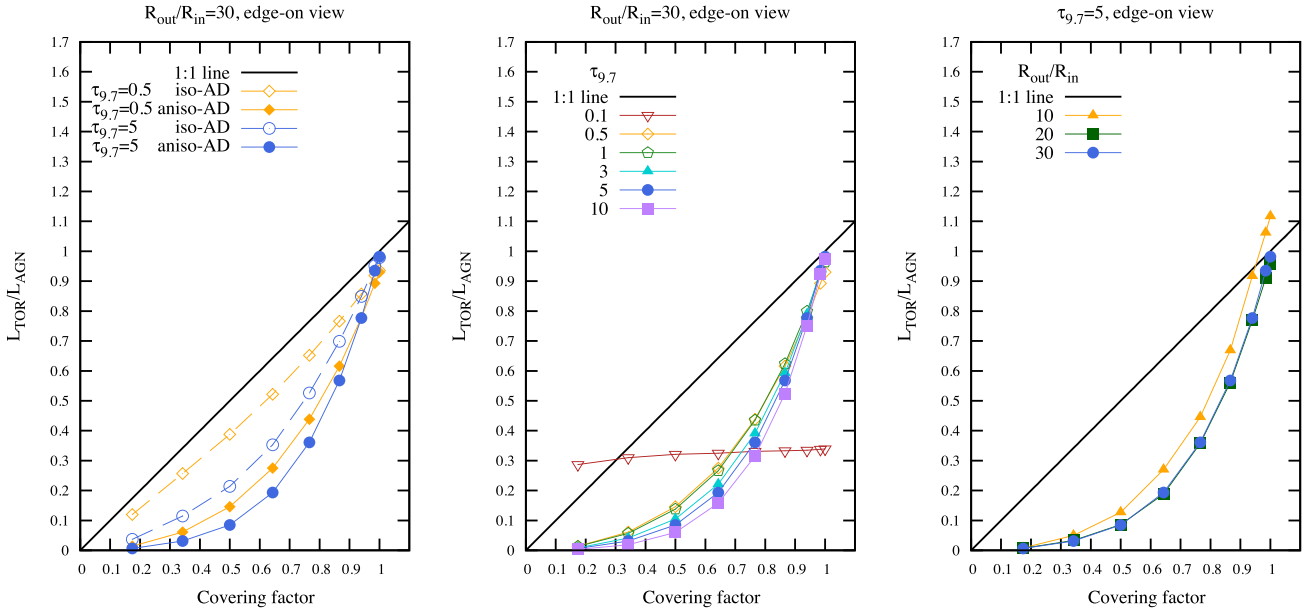

Figure 9. The same as in Fig. 7 but for the case of an edge-on view (type 2 AGN). We note that $L_{\rm torus}/L_{\rm AGN}$ always underestimates CFs, with a weak dependence on the torus parameters.

3.3 $L_{\rm torus}/L_{\rm AGN}$ as a CF proxy: type 2 AGN case

In this section we examine the relation between $L_{\rm torus}/L_{\rm AGN}$ and CF for the type 2 AGN case, following the same approach as in Section 3.2.

3.3.1 The total infrared emission

Fig. 9 is the equivalent of Fig. 7, except that now we are measuring the model SED luminosities for an edge-on view. We look first at the open yellow diamonds in the left-hand panel, which represent the case of an isotropic disc and an MIR thin torus. We note that this line is slightly more offset from the 1:1 identity line than in the type 1 case. Here we need to remember that MIR thin ($\tau_{9.7} = 0.5$) refers to the underlying smooth dust density distribution, before the clumpy two-phase medium is generated (see Section 2.4). The actual optical depth in the two-phase model may vary depending on the number of clumps along the particular line of sight, and even become optically thick, which is the reason for the offset in this case.

Next we examine the open blue circles, corresponding to the case of an isotropic disc surrounded by MIR thick dust. Since in the edge-on view the optically thick structure appears fainter than in the face-on view, using these fluxes we will underestimate $L_{\rm torus}$ and thus the CF.

Moving on to the more realistic disc with anisotropic emission but encompassed by MIR thin dust (solid yellow diamonds), we see that, as dictated by the disc emissivity dependence on polar angle (equation 1), the CFs are severely underestimated.

Finally, in the most realistic case of an MIR thick dust enveloping an anisotropic accretion disc (solid blue circles), based on previous considerations, we can only expect the CFs to be even more underestimated; we see that this is indeed the case.

Now we turn to the central panel of Fig. 9, in which we examine the effect of changing the optical depth. Again, red open triangles represent the case of very low optical depth, which means that the dust is partially transparent to the accretion disc emission, and thus $L_{\rm torus}/L_{\rm AGN}$ cannot be used as CF proxy. As for the other values of the optical depth we have considered, the relations do not diverge much from each other, especially if considering the realistic range of optical depths (solid symbols). From the right-hand panel, we see that there is very little dependence on the $R_{\rm out}/R_{\rm in}$ parameter.

We have so far focused just on models where the dust density does not vary as a function of the polar angle. If, instead, there is a gradient, we can expect some degeneracy with viewing angle (inclination). In Fig. 10 we inspect such a case with parameter $q = 1$ as defined in equation (6). We show only results for type 2 cases, leaving out the combinations of inclinations and CFs that allow direct view of the central engine. For inclination in the range of 60°–90° (measured from the polar axis) the results are within the limits of optically thin to thick cases seen in Fig. 9. Only for tori with high CFs (>0.8), which can provide obscuration for even small inclinations (<50°), there is a significant departure between the $L_{\rm torus}/L_{\rm AGN}$–CF relations for different viewing angles. In the extreme cases, CFs can be even somewhat overestimated.

3.3.2 NIR, MIR and FIR emission as CF proxy

We now inspect Fig. 11 where we can see how luminosities at different wavelength bands act as CF estimators. Like in Fig. 8, we consider NIR (1–5 μm, yellow stars), MIR (5–25 μm, red crosses), FIR (25–380 μm, brown triangles) and total IR (blue circles); from left to right, panels correspond to cases of $\tau_{9.7} = 3, 5, 10$.

We see that with increasing optical depth, the NIR and FIR contributions are going in opposite ways: as contribution from hot dust is decreasing and becoming negligible, cold dust contribution rises and becomes comparable to that from warm (MIR) dust. The caveats mentioned in the Section 3.2.2 – contamination by sources in the NIR and FIR other than AGN and the need for disentangling different components by spectral energy decomposition – are to be kept in mind here as well. As such, neither NIR nor FIR luminosities

Downloaded from http://mnras.oxfordjournals.org/ at UNIVERSIDAD DE CHILE on August 9, 2016

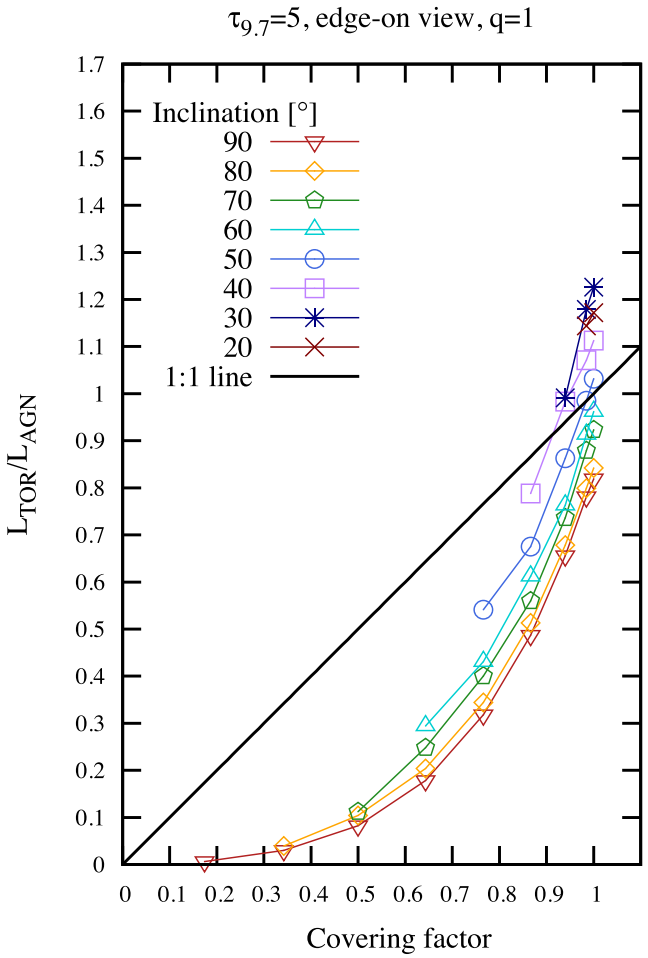

Figure 10. Similar as in the central panel of Fig. 9 but only for $\tau_{9.7} = 5$ and $q = 1$, i.e. with a gradient in dust density with polar angle (see equation 6). Only combinations of CFs and viewing angles that have dust-intercepting lines of sight (i.e. type 2 AGN cases) are plotted. We see that even when the gradient is present, the resulting CFs are still within the limits of optically thin to thick cases. The exception are tori with high CFs (>0.7), which can provide obscuration for even small inclinations; in this case, CFs could be overestimated.

are reliable CF proxies. On the other hand, in the case of type 2 AGNs, MIR luminosity is a much more robust CF estimator, as its contribution remains almost constant with increasing optical depth.

3.4 The case of misaligned accretion disc and dusty torus

In all the results so far presented, we were assuming that the accretion disc and the dusty torus are aligned. This is a reasonable assumption if both the disc and the torus have an origin in the same accretion event, i.e. the same material arriving from larger scales to the vicinity of the black hole. An AGN can also be fueled by a series of such events coming in from random directions. When this happens a partial re-alignment of the newly arriving material and the old accretion disc must occur, producing a warped structure. Lawrence & Elvis (2010) suggested that such a warped structure can provide the necessary CF. Detailed hydrodynamical simulations coupled with radiative transfer are needed to explore the evolution of such a structure. However, it is reasonable to assume that the accretion disc is able to partially clear out its close environment by dust sublimation, radiation pressure and winds, which would effectively reduce the misalignment with the dusty structure. In the remaining of this section, we will consider a case of a misaligned accretion disc and dusty obscuring structure, and study how this misalignment affects the CF estimates.

Unfortunately, precise estimates of inclination of the accretion disc and the dusty torus are available only for nearby sources that can be resolved at different wavelength regimes, and even then they may not be reliable. Usually, the position angles of the jet, ionization cone, maser disc and IR-emitting structure are used to estimate the orientation of the accretion disc and the dusty obscuring structure. The jet is assumed to be launched from the vicinity of the black hole, perpendicular to the disc. It is commonly believed that launching of the jet is related to the spin of the black hole, which is determined by the sum of angular momentums of all the accreting events in the past of an AGN. In that case, the presence of a strong and linear jet rules out multiple accreting events from random directions, as they would in a net effect reduce the spin of the black hole. In this scenario we expect that the disc-torus misalignment, if present, must be limited to rather small values.

In the case of NGC 1068, there is a systematic change of orientation with radius. Summarizing the discussion from Lawrence & Elvis (2010), the inner radio jet is orthogonal to the polarization angle; the inner maser disc is misaligned with respect to the jet by 20°, while the outer maser disc is misaligned by 40°. The outer radio jet is aligned with the narrow line region and both are misaligned with the inner jet by ≈20°. Finally, Raban et al. (2009) conclude that the current phase of the AGN in NGC 1068 is not likely to have significant effect on the black hole spin (and thus the orientation of the jet), and that it is the angular momentum of the infalling material together with the gravitational potential of the nucleus, that are responsible for the current orientation of the maser, the accretion disc and the dusty torus. From similar considerations in the case of Circinus, a misalignment between the accretion disc and the dusty structure of ≈27° is inferred (Greenhill et al. 2003; Tristram et al. 2007, 2014). In a sample of 21 local objects, Asmus et al. (submitted) studied the orientation between the resolved MIR elongated emission (tentatively interpreted as the inner funnel of an extended dust distribution) and the AGN axis inferred by different methods. They found that in 18 objects the MIR emission is aligned with the AGN axis within 35°, and in 9 of those within 18°; the median angular difference for the whole sample is 19° with a standard deviation of 27°.

Having in mind all said above, we conclude that, while the estimates of the orientation between the accretion disc and the dusty structure remain uncertain and with a lot of caveats, the eventual misalignment is likely to be confined to up to ≈30°.

To investigate effect of misalignments on the CF estimates, we carried out two additional sets of simulations, identical to those discussed previously, but with the accretion disc inclined by 15° and 30° with respect to the dusty torus. The resulting dust CF estimates in such systems are presented in Fig. 12. Blue circles represent the previously discussed case of aligned disc and torus; yellow stars and red crosses stand for the cases of disc inclined by 15° and 30°, respectively. Looking at the face-on case (left-hand panel), we see that for $i_{\rm disk} = 15°$ the change in estimated CFs is marginal. For $i_{\rm disk} = 30°$ the change is more significant. All the values are systematically higher than in the case of alignment; for lower CFs, they almost lie on the 1:1 line. This is a consequence of the anisotropic disc emission: the more the disc is inclined, the more radiation will be reprocessed by the dust, resulting in higher IR

Downloaded from http://mnras.oxfordjournals.org/ at UNIVERSIDAD DE CHILE on August 9, 2016

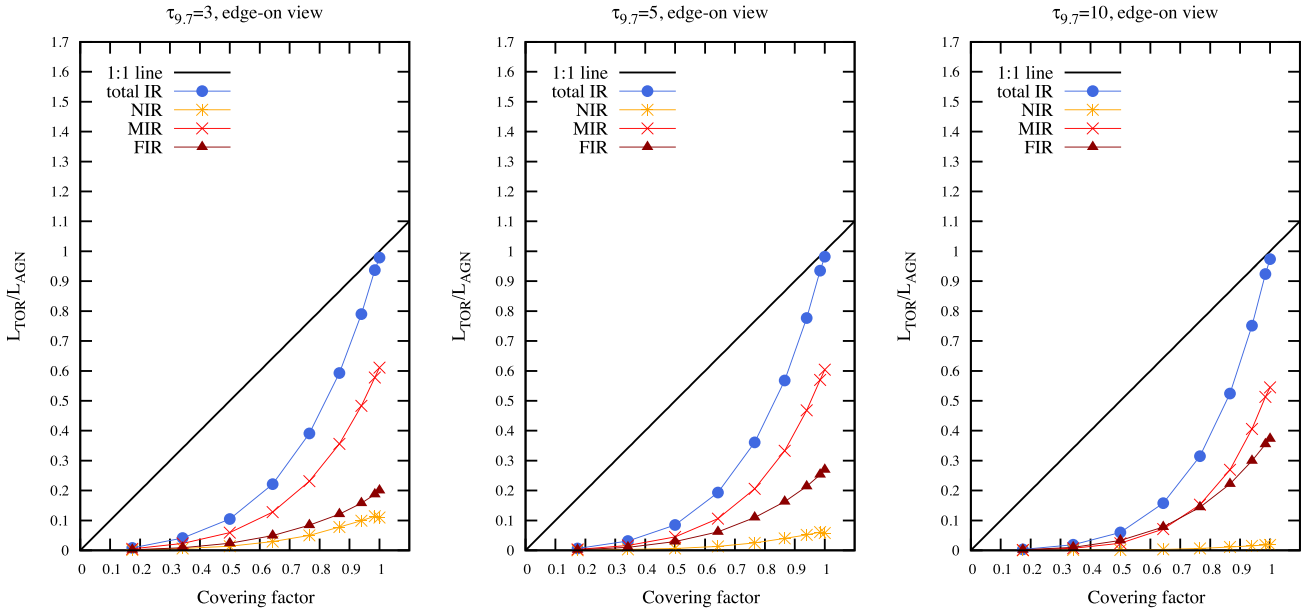

Figure 11. The same as in Fig. 8 but for the case of an edge-on view.

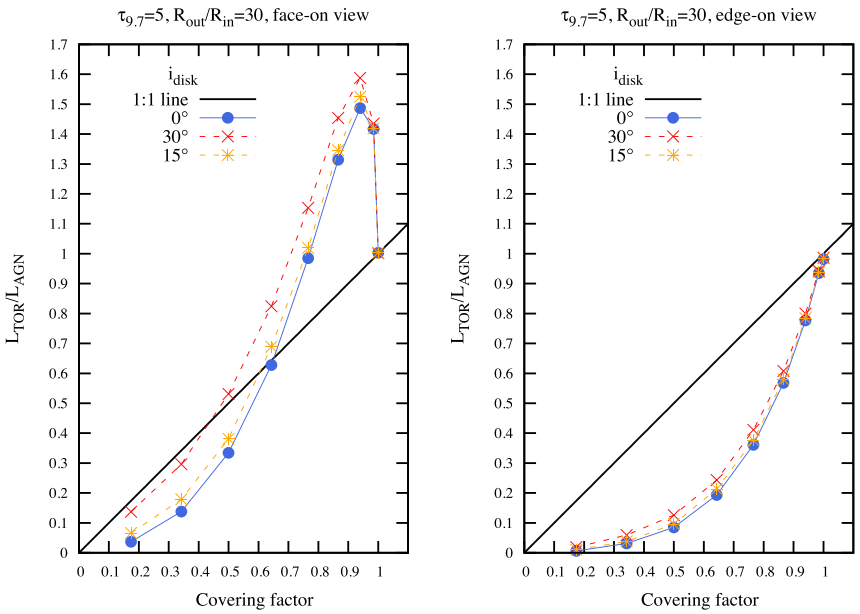

Figure 12. Comparing the CF estimates for aligned (blue circles) and misaligned disc and torus cases. Disc tilted by 15° (yellow stars) yields in a marginal difference. The difference becomes significant at a tilt of 30° (red crosses).

emission, and thus higher CF estimates. In edge-on case (right-hand panel) the misalignment does not play a significant role.

4 IMPLICATIONS FOR INFERRING THE OBSCURED AGN FRACTION

4.1 Obscured AGN fraction versus $L_{\rm AGN}$

Now we will demonstrate a practical use of our results by correcting the observed $L_{\rm torus}/L_{\rm AGN}$ ratio to infer the obscured AGN fraction in two samples taken from the literature. We choose the works of Maiolino et al. (2007) and Lusso et al. (2013), both dealing with type 1 AGNs only. The first work analyses a sample of 58 high-luminosity quasars and low-luminosity AGNs, in a redshift range $2 < z < 3.5$; the second one compiles a sample of 513 type 1 AGNs from the XMM-COSMOS survey ($0.04 < z < 4.25$). We point the reader to the extensive comparison of the two samples and results in Lusso et al. (2013).

Table 1 contains coefficients of the polynomial curve fits,

$$\mathrm{CF} = a_4 R^4 + a_3 R^3 + a_2 R^2 + a_1 R + a_0, \quad (8)$$

to the relations between the CF and $R \equiv L_{\rm torus}/L_{\rm AGN}$ presented in Section 3, and in the central panels of Figs 7 and 9. We provide the coefficients in the range of realistic values of $\tau_{9.7} = 3$–10. As explained in Section 3, the CF $-$ R curves in this range of optical depth values cover the most relevant parameter space, including variations of other torus parameters as well. The CF $-$ R relation was fitted only up to the turn-over point (CF = 0.94), because of the

Downloaded from http://mnras.oxfordjournals.org/ at UNIVERSIDAD DE CHILE on August 9, 2016

Table 1. Coefficients of the polynomial curve fits to the relation between the CF and L_{torus}/L_{AGN} presented in the central panels of Figs 7 and 9, and in Fig. 12 for a straightforward correction of observed luminosity ratio to account for the dusty torus anisotropy. The type 1 sections has an additional column indicating the maximum value of R for which polynomial approximation is valid. For type 2 corrections, R_{max} is 1 in all cases.

$$CF = a_4R^4 + a_3R^3 + a_2R^2 + a_1R + a_0;\ R \equiv L_{torus}/L_{AGN}$$

	type 1						type 2				
$\tau_{9.7}$	a_4	a_3	a_2	a_1	a_0	R_{max}	a_4	a_3	a_2	a_1	a_0
3	−0.177 798	0.875 215	−1.487 27	1.408 27	0.192 478	1.3	0	2.038 66	−3.975 89	2.764 58	0.204 995
5	−0.060 1471	0.474 93	−1.045 46	1.202 18	0.195 615	1.5	0	2.228 44	−4.280 61	2.8593	0.226 25
10	−0.025 5416	0.299 937	−0.782 418	1.026 96	0.196 387	1.7	0	2.501 38	−4.683 18	2.968 75	0.258 279
	$\tau_{9.7} = 5$; the disc and the torus misaligned										
i_{disc}	a_4	a_3	a_2	a_1	a_0	R_{max}	a_4	a_3	a_2	a_1	a_0
15°	−0.084 5587	0.526 976	−1.085 96	1.246 35	0.151 897	1.5	0	2.082 95	−4.073 39	2.809 35	0.209 374
30°	−0.0341 992	0.402 01	−1.064 48	1.400 97	0.003 745	1.6	0	1.948 74	−3.903 22	2.814 42	0.164 062

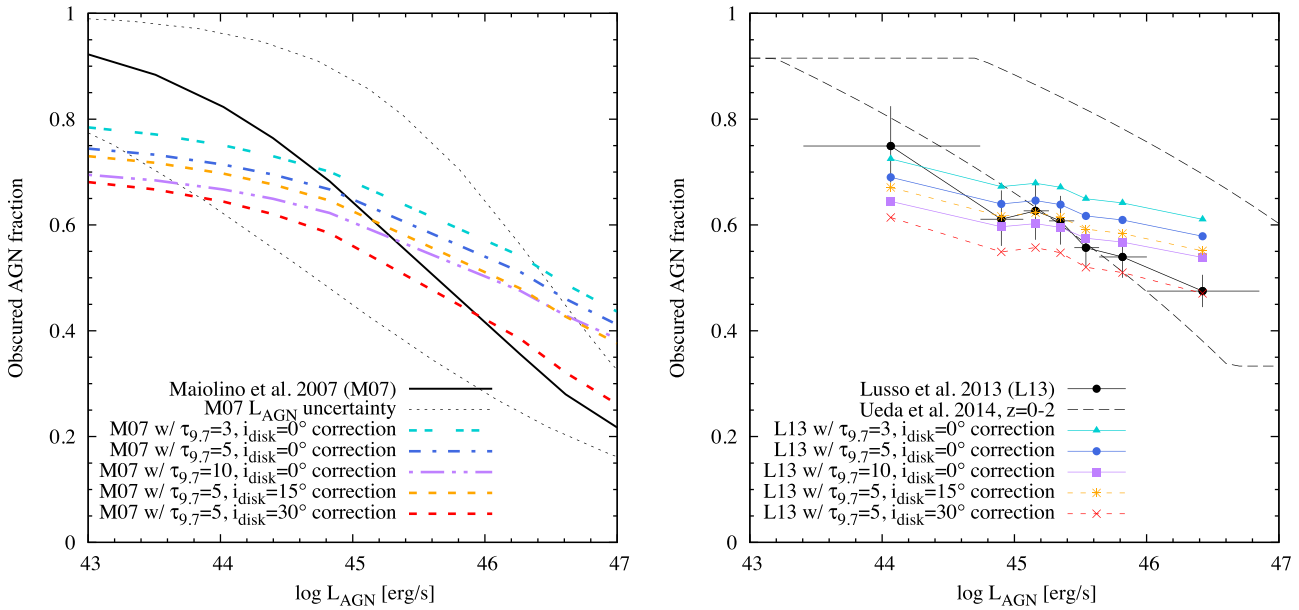

Figure 13. The obscured AGN fraction versus L_{AGN} according to Maiolino et al. (2007) and Lusso et al. (2013) (left- and right-hand panel, respectively, in black solid lines and points), and the same after applying corrections based on our results (coloured lines and symbols). Cyan, blue and violet lines are for a range of realistic optical depths in the case of aligned disc and torus; yellow and red represent cases with misalignment. The dotted black lines in the left-hand panel indicate the uncertainties due to the bolometric correction used in Maiolino et al. (2007); uncertainty bars in the right-hand panel represent 1σ of the distribution found by Lusso et al. (2013). Uncertainties in the corrected cases are omitted for the clarity of the plot. Long-dashed black lines in the right-hand panel are the prediction from the AGN population synthesis model by Ueda et al. (2014) calculated at $z = 0$ (lower line) and $z \geq 2$ (upper line). We notice that the trend of decreasing fraction of obscured AGNs with increasing luminosity becomes much less steep than in original data.

non-uniqueness of the relation beyond that point. As discussed in Section 3.2, this would have only a marginal effect on observational results, as there is an extremely small probability that AGNs with such high CFs would be observed through the dust-free cone and classified as type 1s.

In Fig. 13 we show the obscured AGN fraction versus L_{AGN} from Maiolino et al. (2007) (left) and Lusso et al. (2013) (right), with solid black lines and points. The data we took are for the case the authors refer to as 'optically thin', i.e. before applying the simple, analytical anisotropy correction factor (equation 3 in Lusso et al. 2013). Both works found a decrease of the obscured AGN fraction with increasing L_{AGN}. Having a quick look back at Fig. 7, we remind ourselves that in the case of type 1 AGNs the dusty torus and the accretion disc anisotropies conspire to make L_{torus}/L_{AGN} underestimate low CFs, and overestimate high CFs. The simple expression in equation (8) with coefficients in Table 1 allow us to straightforwardly correct the observed luminosity ratio. The coloured lines and symbols in Fig. 13 represent the obscured AGN fraction after we applied the corrections from this work, for different optical depths (cyan, blue, violet) and disc-torus orientation (orange and red). We see that the actual trend of obscured fraction with L_{AGN} is less steep than it originally appeared. We recover similar values as Maiolino et al. (2007) and Lusso et al. (2013) around $L_{AGN} \approx 10^{45}$ erg/s, and have significant deviations at low and high L_{AGN} ends. Note that there are considerable uncertainties in the bolometric correction factor for L_{AGN} and dispersion of the obscured fraction around their median values. However, our approach allow us to put tighter limits on the obscured AGN fraction, compared to the limiting cases of 'optically thin and thick' regimes discussed by the former studies (see fig. 10 a in Lusso et al. 2013). If we consider Lusso et al. (2013) results with our individual corrections, the dust CF of AGNs depend veary weakly on L_{AGN}, with values in the range CF $\approx$ 0.6–0.7, depending on the employed correction. Note that the choice of the correction factors

Downloaded from http://mnras.oxfordjournals.org/ at UNIVERSIDAD DE CHILE on August 9, 2016

scales the results along the y-axis, while the slope remains almost unchanged.

Netzer et al. (2016) found that CFs are basically independent of AGN luminosity and suggest that earlier results inferring steeper dependence of IR-derived CFs on $L_{\rm AGN}$ may be biased by the inconsistent use of various bolometric correction factors. The goal of this work is to illustrate effects of the torus anisotropy and provide a method to properly correct for it; we do not attempt to revise the $L_{\rm AGN}$ estimates. In the case Netzer et al. refer to as 'isotropic' (before analytical anisotropy correction factor is applied), they found the median covering factor of CF = 0.68. As we have shown, for moderate optical depths in MIR, $L_{\rm torus}/L_{\rm AGN}$ is a very good indicator of the CFs in the range of CF $\approx$ 0.65–0.7. Thus, if we would apply our corrections to the obscured AGN fraction found by Netzer et al., their results would not change considerably. In fact, the very mild trends which might still be present within uncertainties, would become even flatter. However, Netzer et al. sample is in a narrower luminosity range and at and almost without overlapping to those of Maiolino et al. (2007) and Lusso et al. (2013). Given that the different methods are used to estimate $L_{\rm AGN}$ in these works, further comparison between them would be precarious. It should be kept in mind that considerable observational uncertainties still remain, and changes of the CF could still be present and hidden within the uncertainties; but the change would be limited to less than a factor of 2 over more than 3 orders of magnitude in $L_{\rm AGN}$.

4.2 The discrepancy between the obscured AGN fraction inferred from IR and X-rays

The decrease of the CF of the torus with increasing luminosity is systematically found in X-ray surveys (e.g. Ueda et al. 2003; Beckmann et al. 2009; Burlon et al. 2011; Ricci et al. 2013; Merloni et al. 2014; Ueda et al. 2014; Buchner et al. 2015). In the most complete study of local AGNs, Ricci et al. (2015) reconstructed the intrinsic column density ($N_{\rm H}$) in two luminosity bins and found that the intrinsic fraction of both Compton-thin and Compton-thick objects decreases with $L_{\rm AGN}$. Such trends may be interpreted as an indirect signature of AGN feedback, in a sense that more luminous sources are able to clear out their immediate environment (obscuring region) more efficiently through radiation pressure, winds, dust sublimation and photoionization (see e.g. the radiation-driven fountain scenario by Wada 2015). However, there appears to be a discrepancy between the obscured AGN fraction found by X-ray studies and inferred from $L_{\rm torus}/L_{\rm AGN}$. Our revised results based on IR suggest: (a) obscured AGN fraction with very weak dependence on $L_{\rm AGN}$, and (b) larger fraction of obscured high-luminosity AGNs than those estimated from X-ray surveys below 10 keV (Hasinger 2008).

The tension is reduced if we take into account the presence of AGNs with Compton-thick absorbers that are required in population synthesis models of the Cosmic X-ray background (CXB), but that are missed by surveys of individual sources (e.g. Ueda et al. 2014). The two dashed lines in Fig. 13 (right) are the predictions based on the AGN population synthesis model by Ueda et al. (2014) calculated at $z = 0$ (lower line) and $z \geq 2$ (upper line). Here we convert the bolometric luminosity to the X-ray luminosity (2–10 keV) by using the luminosity-dependent bolometric correction factors given in Hopkins, Richards & Hernquist (2007). Then, we calculate the obscured fraction with $N_{\rm H} > 10^{22}$ cm^{-2} including Compton-thick AGNs from the absorption function of Ueda et al. (2014), which is dependent both on X-ray luminosity and redshift. We see that obscured AGN fractions at high luminosities ($\gtrsim L_{\rm AGN} 10^{45}$ erg s^{-1}) with corrections for low and moderate optical depth fall within the region between the two boundaries. The tension remains at lower luminosities, but the redshift–luminosity coupling in the Lusso et al. (2013) sample must be taken into account for detailed analyses. The agreement with the CXB model predictions is better if a subsample excluding highly reddend AGNs from Lusso et al. (2013) is adopted. These highly reddend objects might have understimated $L_{\rm torus}$ and thus, CFs as well. In the subsample with $E(B-V) \leq 0.1$, inferred CFs are higher than in the total sample, by about 0.1. Note that the slope of the CXB model is much flatter than those found in X-ray surveys (e.g. Hasinger 2008) because of (a) the inclusion of Compton-thick AGNs, whose number is the same as that of Compton-thin absorbed AGNs in the Ueda et al. (2014) model, and of (b) the non-linear relation between the bolometric and X-ray luminosities (e.g. Hopkins et al. 2007). In addition, the positive correlation between luminosity and redshift in the sample would work to flatten the observed slope because higher obscured fractions are expected at higher redshifts (hence higher luminosities).

Based on their IR-derived CFs, Treister et al. (2008) also suggest a significant population of heavily obscured AGNs missed by X-ray observations. There are a number of other causes that could contribute to the discrepancy between IR and X-ray studies. Mayo & Lawrence (2013) explore a scenario in which many objects are partially covered by Compton-thick material, and partially by intermediately thick material. Such objects would appear as Compton-thin, but with suppressed X-ray luminosity, artificially producing correlation of obscured fraction with luminosity. This does not pose a problem when data of sufficient quality is available, as then obscuration can be properly modelled. However, this is often not the case in large AGN surveys. Mayo & Lawrence (2013) suggest that the observed trend can be reproduce in a model where 33 per cent of AGN are unobscured, 30 per cent are heavily buried, and 37 per cent have a range of intermediate partial coverings. On the other hand, if type 2 AGNs were systematically obscured by partially covering Compton-thick material, one would expect that the ratio between the Fe $K_{\rm alpha}$ line and the 10–50 keV luminosity would be larger for type 2s than for type 1s, which is the contrary of what is observed (e.g. Ricci et al. 2014). Other possible causes include a number of selection effects or unaccounted biases. Sazonov, Churazov & Krivonos (2015) showed that, apart from the negative bias in finding obscured AGN in hard X-ray flux limited surveys due to the absorption in the torus, there is also positive bias in finding unobscured AGN, due to Compton reflection in the torus. They demonstrate that these biases should inevitably lead to smaller obscured AGN fraction in the high-luminosity end than in the low-luminosity end, even if the obscured AGN fraction has no intrinsic luminosity dependence. They also show that if the central X-ray source has a certain degree of anisotropy ($\sim\cos\theta$), the intrinsic obscured AGN fraction could be consistent with a luminosity-independent torus CF. Further discussions on this and related issues can be found in Merloni et al. (2014) and Netzer (2015).

Finally, the discrepancy could be a hint that the IR-emitting obscurer and the X-ray absorbing material may have different CFs, owing to still poorly understood physics of dust and gas dynamics in a presence of a strong radiation field. Further work is needed to fully understand and resolve this issue.

5 CONCLUSIONS

We conducted a comprehensive investigation of the $L_{\rm torus}/L_{\rm AGN}$ ratio as a dust CF estimator in AGNs. Using SKIRT, a state-of-the-art 3D Monte Carlo radiative transfer code, we have calculated

Downloaded from http://mnras.oxfordjournals.org/ at UNIVERSIDAD DE CHILE on August 9, 2016

a grid of SEDs emitted by the clumpy two-phase dusty structure surrounding the central engine ('the dusty torus'). With this grid of SEDs at hand, we studied the relation between the aforementioned luminosity ratio and the actual CF for different parameters of the torus. In this approach, anisotropies introduced by the nature of the accretion disc emission and by the complex interplay of different parameters during the transfer of radiation through the dust are taken into account.

We found that the combined effects of anisotropic emission of the dusty torus and the accretion disc lead to:

(i) $L_{\rm torus}/L_{\rm AGN}$ underestimating low CFs and overestimating high CFs in case of type 1 AGNs

(ii) $L_{\rm torus}/L_{\rm AGN}$ always underestimating CFs in case of type 2 AGNs.

Our results provide a new way to correct the observed $L_{\rm torus}/L_{\rm AGN}$ to account for the anisotropies and to recover the actual CFs. We demonstrated the consequences of our findings for inferring the fraction of obscured AGNs, using the samples from the literature.

In particular, our results suggest that:

(i) obscured AGN fraction depends more weakly on $L_{\rm AGN}$ than previously thought, with CF values in range CF $\approx$ 0.6–0.7

(ii) there is a larger fraction of obscured high-luminosity AGNs than that estimated from X-ray surveys.

We show that the larger fraction of obscured high-luminosity AGNs may be consistent with the presence of Compton-thick AGNs that are not included in analyses of absorbed AGN fraction using X-ray selected samples. The tension still remains at low luminosities. Further investigation is warranted to fully resolve the discrepancy.

We emphasize that all the conclusions are consequence of just following two assumptions: (a) functional form of the accretion disc luminosity dependence on polar angle, and (b) the dusty structure surrounding the disc is of moderate- to high optical thickness in the MIR. The former assumption is certainly satisfied if the disc is geometrically thin. We showed that the second assumption must be satisfied as well for the typical dusty structures in AGNs, as otherwise the 10 μm silicate feature would be commonly appearing in emission (or at very least not in absorption) even in type 2 objects. Thus, as long as the two above mentioned conditions are met, our results hold up even if the exact geometry of the obscuring dusty material is different than assumed in this work (flared-disc).

Finally, we provide for the community polynomial function approximation of the relation between the CF and $L_{\rm torus}/L_{\rm AGN}$, which allows for a straightforward way to correct the observed luminosity ratio and obtain actual dust CFs. We encourage colleagues to contact us if they should require correction functions for a specific sets of parameters.

ACKNOWLEDGEMENTS

We thank the anonymous referee for useful comments and suggestions. MS is indebted to Peter Camps for continuous support and development of the SKIRT code and thankful to Daniel Asmus and Konrad Tristram for careful reading and comments on the manuscript. MS acknowledges support by FONDECYT through grant no. 3140518 and by the Ministry of Education, Science and Technological Development of the Republic of Serbia through the projects Astrophysical Spectroscopy of Extragalactic Objects (176001) and Gravitation and the Large Scale Structure of the Universe (176003). MS and CR acknowledge support from the Japanese Society for the promotion of Science (JSPS), through projects no. PE14042 and 12795, respectively. CR acknowledges financial support from CONICYT-Chile grants 'EMBIGGEN' Anillo ACT1101, FONDECYT 1141218 and Basal-CATA PFB–06/2007. JF acknowledges the financial support from the grant UNAM-DGAPA-PAPIIT IA104015. Powered@NLHPC: this research was partially supported by the supercomputing infrastructure of the NLHPC (ECM-02).

REFERENCES

Alonso-Herrero A. et al., 2011, ApJ, 736, 82
Antonucci R., 1993, ARA&A, 31, 473
Assef R. J. et al., 2013, ApJ, 772, 26
Baes M., Camps P., 2015, Astron. Comput., 12, 33
Baes M. et al., 2003, MNRAS, 343, 1081
Baes M. et al., 2010, A&A, 518, L39
Baes M., Verstappen J., De Looze I., Fritz J., Saftly W., Vidal Pérez E., Stalevski M., Valcke S., 2011, ApJS, 196, 22
Barvainis R., 1987, ApJ, 320, 537
Beckmann V. et al., 2009, A&A, 505, 417
Buchner J. et al., 2015, ApJ, 802, 89
Burlon D., Ajello M., Greiner J., Comastri A., Merloni A., Gehrels N., 2011, ApJ, 728, 58
Camps P., Baes M., 2015, Astrono. Comput., 9, 20
Camps P., Baes M., Saftly W., 2013, A&A, 560, A35
Capellupo D. M., Netzer H., Lira P., Trakhtenbrot B., Mejía-Restrepo J., 2015, MNRAS, 446, 3427
Davis S. W., Laor A., 2011, ApJ, 728, 98
De Geyter G. et al., 2015, MNRAS, 451, 1728
De Looze I., Baes M., Fritz J., Verstappen J., 2012a, MNRAS, 419, 895
De Looze I. et al., 2012b, MNRAS, 427, 2797
Deo R. P., Richards G. T., Nikutta R., Elitzur M., Gallagher S. C., Ivezić Ž., Hines D., 2011, ApJ, 729, 108
Fritz J., Franceschini A., Hatziminaoglou E., 2006, MNRAS, 366, 767
Greenhill L. J. et al., 2003, ApJ, 590, 162
Hasinger G., 2008, A&A, 490, 905
Hatziminaoglou E., Fritz J., Franceschini A., Afonso-Luis A., Hernán-Caballero A., Pérez-Fournon I., Serjeant S. et al., 2008, MNRAS, 386, 1252
Hatziminaoglou E., Fritz J., Jarrett T. H., 2009, MNRAS, 399, 1206
Hatziminaoglou E. et al., 2010, A&A, 518, L33
Hönig S. F., Kishimoto M., 2010, A&A, 523, A27
Hopkins P. F., Richards G. T., Hernquist L., 2007, ApJ, 654, 731
Hubeny I., Blaes O., Krolik J. H., Agol E., 2001, ApJ, 559, 680
Ivezic Z., Elitzur M., 1997, MNRAS, 287, 799
Kishimoto M., Hönig S. F., Beckert T., Weigelt G., 2007, A&A, 476, 713
Krawczyk C. M., Richards G. T., Mehta S. S., Vogeley M. S., Gallagher S. C., Leighly K. M., Ross N. P., Schneider D. P., 2013, ApJS, 206, 4
Laor A., Draine B. T., 1993, ApJ, 402, 441
Lawrence A., Elvis M., 2010, ApJ, 714, 561
Leighly K. M., Cooper E., Grupe D., Terndrup D. M., Komossa S., 2015, ApJ, 809, L13
Li A., Draine B. T., 2001, ApJ, 554, 778
Lira P., Videla L., Wu Y., Alonso-Herrero A., Alexander D. M., Ward M., 2013, ApJ, 764, 159
Lusso E. et al., 2013, ApJ, 777, 86
Lynden-Bell D., 1969, Nature, 223, 690
Maiolino R., Shemmer O., Imanishi M., Netzer H., Oliva E., Lutz D., Sturm E., 2007, A&A, 468, 979
Marconi A., Risaliti G., Gilli R., Hunt L. K., Maiolino R., Salvati M., 2004, MNRAS, 351, 169
Markowitz A. G., Krumpe M., Nikutta R., 2014, MNRAS, 439, 1403
Mateos S. et al., 2015, MNRAS, 449, 1422
Mateos S. et al., 2016, ApJ, accepted
Mathis J. S., Rumpl W., Nordsieck K. H., 1977, ApJ, 217, 425
Mayo J. H., Lawrence A., 2013, MNRAS, 434, 1593
Merloni A. et al., 2014, MNRAS, 437, 3550

Downloaded from http://mnras.oxfordjournals.org/ at UNIVERSIDAD DE CHILE on August 9, 2016

Molinari S. et al., 2011, ApJ, 735, L33
Monaghan J. J., Lattanzio J. C., 1985, A&A, 149, 135
Mor R., Netzer H., 2012, MNRAS, 420, 526
Mor R., Trakhtenbrot B., 2011, ApJ, 737, L36
Mor R., Netzer H., Elitzur M., 2009, ApJ, 705, 298
Netzer H., 1987, MNRAS, 225, 55
Netzer H., 2015, ARA&A, 53, 365
Netzer H. et al., 2016, ApJ, in press
Polletta M., Weedman D., Hönig S., Lonsdale C. J., Smith H. E., Houck J., 2008, ApJ, 675, 960
Ponti G., Morris M. R., Terrier R., Goldwurm A., 2013, in Torres D. F., Reimer O., eds, Astrophysics and Space Science Proc. 34, Cosmic Rays in Star-Forming Environments. Springer, Berlin, p. 331
Popović L. Č., Jovanović P., Stalevski M., Anton S., Andrei A. H., Kovačević J., Baes M., 2012, A&A, 538, A107
Raban D., Jaffe W., Röttgering H., Meisenheimer K., Tristram K. R. W., 2009, MNRAS, 394, 1325
Ramos-Almeida C. et al., 2011, ApJ, 731, 92
Ricci C., Paltani S., Awaki H., Petrucci P.-O., Ueda Y., Brightman M., 2013, A&A, 553, A29
Ricci C., Ueda Y., Paltani S., Ichikawa K., Gandhi P., Awaki H., 2014, MNRAS, 441, 3622
Ricci C., Ueda Y., Koss M. J., Trakhtenbrot B., Bauer F. E., Gandhi P., 2015, ApJ, 815, L13
Roseboom I. G., Lawrence A., Elvis M., Petty S., Shen Y., Hao H., 2013, MNRAS, 429, 1494
Runnoe J. C., Brotherton M. S., Shang Z., 2012, MNRAS, 422, 478
Saftly W., Camps P., Baes M., Gordon K. D., Vandewoude S., Rahimi A., Stalevski M., 2013, A&A, 554, A10
Saftly W., Baes M., Camps P., 2014, A&A, 561, A77
Sazonov S., Churazov E., Krivonos R., 2015, MNRAS, 454, 1202
Shen Y. et al., 2011, ApJS, 194, 45
Slone O., Netzer H., 2012, MNRAS, 426, 656
Springel V., 2010, ARA&A, 48, 391
Stalevski M., Fritz J., Baes M., Popovic L. C., 2012a, in Mason R., Alonso-Herrero A., Packham C., eds, Torus Workshop. Univ. Texas, San Antonio, p. 170
Stalevski M., Fritz J., Baes M., Nakos T., Popović L. Č., 2012b, MNRAS, 420, 2756
Stalevski M., Jovanović P., Popović L. Č., Baes M., 2012c, MNRAS, 425, 1576
Trakhtenbrot B., Netzer H., 2012, MNRAS, 427, 3081
Treister E., Krolik J. H., Dullemond C., 2008, ApJ, 679, 140
Tristram K. R. W. et al., 2007, A&A, 474, 837
Tristram K. R. W., Burtscher L., Jaffe W., Meisenheimer K., Hönig S. F., Kishimoto M., Schartmann M., Weigelt G., 2014, A&A, 563, A82
Ueda Y., Akiyama M., Ohta K., Miyaji T., 2003, ApJ, 598, 886
Ueda Y., Akiyama M., Hasinger G., Miyaji T., Watson M. G., 2014, ApJ, 786, 104
Wada K., 2012, ApJ, 758, 66
Wada K., 2015, ApJ, 812, 82
Wada K., Papadopoulos P. P., Spaans M., 2009, ApJ, 702, 63
Weingartner J. C., Draine B. T., 2001, ApJ, 548, 296

This paper has been typeset from a TEX/LATEX file prepared by the author.

Downloaded from http://mnras.oxfordjournals.org/ at UNIVERSIDAD DE CHILE on August 9, 2016